Identification and Compensation of Torque Ripple in High-Precision Permanent Magnet Motor Drives

Joachim Holtz, *Fellow, IEEE, and Lothar Springob*
University of Wuppertal,
42097 Wuppertal – Germany

Abstract — **Permanent magnet synchronous machines generate parasitic torque pulsations owing to distortion of the stator flux linkage distribution, variable magnetic reluctance at the stator slots, and secondary phenomena. The consequences are speed oscillations which, although small in magnitude, deteriorate the performance of the drive in demanding applications. The parasitic effects are analysed and modelled using the complex state-variable approach. A fast current control system is employed to produce high-frequency electromagnetic torque components for compensation. A self-commissioning scheme is described which identifies the machine parameters, particularly the torque ripple functions which depend on the angular position of the rotor. Variations of permanent magnet flux density with temperature are compensated by on-line adaptation. The algorithms for adaptation and control are implemented in a standard microcontroller system without additional hardware. The effectiveness of the adaptive torque ripple compensation is demonstrated by experiments.**

1. Introduction

AC machines with permanent magnet excitation are used with preference for applications in high-performance positioning systems and machine tool spindle drives. They enjoy the unique advantage that the absence of separate excitation windings or magnetizing currents reduces the copper losses considerably. The high efficiency of permanent magnet machines permits a totally enclosed design with surface cooling. The use of rare-earth permanent magnets enables high flux densities in the airgap, facilitating the construction of motors of unsurpassed power density. A rapid dynamic response is ensured by a high torque-to-inertia ratio, which is achieved using a slim rotor, or a disc-type rotor construction. These favorable properties make the permanent magnet motor an extremely fast, compact and robust mechanical actuator.

A persisting problem with permanent magnet machines is the nonuniformity of the developed torque. The machine torque changes periodically as the rotor advances during its rotation. The resulting torque ripple is caused by deviations from a sinusoidal flux density distribution around the airgap, by deficiencies of feasible winding geometries, and by the variable magnetic reluctance of the airgap due to the stator slots. The feeding power converter also contributes to the torque ripple owing to time harmonics in the current waveforms and to time-varying delays between the commanded and the actual current. According to *Jahns* [1], "no techniques have been reported which can entirely eliminate the presence of these fast torque transients under all operating conditions".

The effects of torque ripple are particularly undesirable in some demanding motion control and machine tool applications. They lead to speed oscillations which cause deterioration in the performance. In addition, the torque ripple may excite resonances in the mechanical portion of the drive system, produce acoustic noise, and, in machine tool applications, leave visible patterns in high-precision machined surfaces.

This paper investigates the different sources of torque ripple in permanent magnet machines. Appropriate models are then defined for the ripple generating mechanisms. A concept for the compensation of torque ripple by a self-commissioning and adaptive control system is presented, and its effectiveness is demonstrated by experimental results.

2. Sources of Torque Ripple

Permanent magnet (PM) machines can be grouped into two categories, depending on their back-emf waveform, which is either trapezoidal or sinusoidal.

2.1 Trapezoidal emf machines

The permanent magnets are mostly fixed to the rotor surface, with groups of axially aligned parallel magnet strips forming the individual machine poles. The airgap flux density is constant under the poles, passing through zero between two poles to assume the opposite direction under the adjacent pole. Ideally, the emf in the distributed stator windings should be trapezoidal, and rectangular stator current waveforms would be required to produce torque which is constant and independent of the respective angular rotor position. In a real machine, the fringing fields at the rotor pole edges cause deviations from the ideal trapezoidal emf waveform. Moreover, the currents are not strictly rectangular. The commutation between the stator phase windings requires finite time intervals, during which the torque magnitude changes considerably [1, 2]. The dips of the torque magnitude may reach up to 25% of rated torque [3]. The torque changes occur periodically in synchronism with the revolving rotor.

2.2 Sinusoidal emf machines

Sinusoidal flux density distribution around the airgap is difficult to achieve in a PM machine. What is important, however, is the resulting flux linkage with the stator winding. Its spatial distribution can be adjusted by an appropriate stator winding geometry such that sinusoidal induced voltage waveforms are achieved with good accuracy. Unlike the trapezoidal PM motor, the sinusoidal version operates as a revolving field machine and requires sinusoidal

IEEE Transactions on Industrial Electronics, Vol. 43, No. 2, 1996, pp. 309-320.

voltage and current waveforms in the stator. The principal torque component is proportional to the quadrature component of the armature current. Magnetic saliency of the rotor produces a reluctance torque component which is low in a PM machine as the saliency is typically low. The reluctance torque is proportional to the product of the quadrature current component i_q and the direct-axis current component i_d. There are harmonic torque components in addition, which result from residual nonsinusoidal flux linkages and from current waveform distortions. In total, the torque ripple of a sinusoidal PM machine is much less than that of a trapezoidal machine. Hence preference is given to sinusoidal PM machines for drives with ultimate performance requirements. The following discussion concentrates on the sinusoidal type of machine.

2.3 Stator slot harmonics and secondary effects

Another cause for torque harmonics is the variable magnetic reluctance in the airgap, which changes periodically when the stator teeth pass by the edges of the rotor magnets. Skewing the stator slots efficiently reduces stator slot ripple, although not completely. Residual torque pulsations occur at a frequency $f_{sl} = \omega N_{sl}$, which increases as the mechanical speed ω increases. N_{sl} is the number of slots. Torque harmonics of lower frequency result from the interaction between unbalanced magnetization of the individual rotor poles with rotor eccentricity.

Flux linkage harmonics can reach typically 2 – 4% of the rated torque, slot harmonics about 3%. The characteristic pattern of machine-produced harmonic torque may substantially differ even when comparing identical machines from the same production batch. In a given machine, this pattern varies with temperature, also irreversibly as in the case of Nd-Fe-B magnets, or following a current overload. The predominant ripple frequency component is six times the stator frequency. Since speed fluctuations due to low frequency torque ripple are automatically compensated by the drive control system, the critical torque harmonics range typically from 100 Hz – 2 kHz. Harmonics of higher frequency are sufficiently attenuated by the rotor inertia.

2.4 Time harmonics

Time harmonics are caused by current waveform distortions in the feeding power converter. To minimize their effect, the switching frequency must be high, and the pulsewidth modulation scheme must not generate subharmonic currents [4]. The influence of the current dependent switching delay time (dead-time effect) must be minimized [5].

3. Review of Earlier Work

The torque ripple content in sinusoidal PM machines can be reduced using specific layouts of the three-phase stator winding, [6]. Also an adequate choice of the relative width of the magnet poles and a particular airgap profile under the poles have an effect on the flux linkage distribution which leads to a reduction of undesired torque ripple [7].

Torque variations of very low frequency are normally eliminated by the speed control system. Torque harmonics of higher frequency can be compensated in principle by generating an inverse torque component through appropriate modulation of the stator current. The compensating current can be obtained in different ways. Most of the existing proposals are based on the evaluation of the back-emf waveform.

A method which relies on the manufacturing data of the motor is presented in [8]. The approach is based on the assumption that the airgap is uniform and that magnetic material is homogeneously magnetized. Manufacturing tolerances and modelling errors will generally influence the flux density distributions to differ from those of a typical machine, or the actual machine, respectively. The ripple compensation is then incomplete.

A different approach is based on the Fourier analysis of the torque equation, from which the required current compensation terms are synthesized, or on the Fourier analysis of the back-emf waveform [9, 10, 11, 12, 13]. The computations are done off-line based on machine data measured on a test bench. The synthesized compensation waveform is valid only for a particular machine.

A simpler method for off-line calculation of the compensation currents is based on the measured trajectory of the back-emf space vector in rotor coordinates [14].

None of these methods are suited for automated the acquisition of stator slot harmonics, a prerequisite for the implementation in industrial drive systems.

Very fast current controllers are required for the practical implementation, as the torque harmonic frequencies increase proportional to the speed. Conventional PI controllers may exhibit bandwidth limits and are not suited to cover the full range of ripple frequencies. Feedforward techniques have been proposed in an effort to overcome the limited bandwidth of PI current control systems [15]. The feedforward signals are read from memory tables which are addressed by the respective values of the state variables. The tables are preprogrammed based on off-line calculations that make use of the differential equation of the motor, but do not include the harmonic phenomena. A large number of EPROMs are required to store the solutions of the pertinent equations.

The existing methods leave the following problems unsolved:

1. Torque harmonics caused by stator slots and rotor eccentricity do not reflect in the induced voltage and hence are not compensated.
2. Owing to manufacturing tolerances, even identical machines from the same production batch will differ in their back-emf waveforms. This makes the harmonic compensation necessarily incomplete.
3. The permenent magnet properties vary with temperature. Their magnetization may also change due to armature reaction in a current overload situation.
4. The compensation of high frequency torque ripple calls for an extended bandwidth of the current control system.

4. Dynamic model of a PM machine

The design of a permanent magnet motor drive for high performance and minimum torque ripple is based on a machine model representing the harmonic effects. The dynamic analysis is based on the space vector notation. In the stationary reference frame, the voltage equation of the stator winding is

$$\boldsymbol{u}_\mathrm{s}^{(\mathrm{S})} = r_\mathrm{s}\boldsymbol{i}_\mathrm{s}^{(\mathrm{S})} + \frac{d\boldsymbol{\psi}_\mathrm{s}^{(\mathrm{S})}}{d\tau}, \tag{1}$$

where $\boldsymbol{u}_\mathrm{s}$ is the stator voltage, $\boldsymbol{i}_\mathrm{s}$ is the stator current, r_s is the winding resistance, and $\boldsymbol{\psi}_\mathrm{s}$ is the stator flux linkage. The superscript $^{(\mathrm{S})}$ refers to the stationary reference frame. All quantities are normalized by their rated values. Note that time is also normalized, $\tau = \omega_\mathrm{sR} t$, [16], where ω_sR is the nominal stator frequency.

The stator flux linkage is composed of a contribution from the stator current, and of the component $\boldsymbol{\psi}_\mathrm{sf}$ relating to the permanent magnet field of the rotor,

$$\boldsymbol{\psi}_\mathrm{s}^{(\mathrm{S})}(\delta) = \boldsymbol{l}_\mathrm{s}(\delta) * \boldsymbol{i}_\mathrm{s}^{(\mathrm{S})} + \boldsymbol{\psi}_\mathrm{sf}(\delta)^{(\mathrm{S})}, \tag{2}$$

where the saliency of the rotor is expressed by the inductance tensor.

This tensor reflects the influence of the *d*-axis inductance l_d and the *q*-axis inductance l_q in the stator as a function of the angular rotor position *d*.

Since the magnet material in the wide airgap has small permeability and low conductivity, eddy currents at transient operation are negligible. Hence a transient time constant does not really exist.

$$\boldsymbol{l}_\mathrm{s}(\delta)^{(\mathrm{S})} = \begin{vmatrix} \frac{l_\mathrm{d}+l_\mathrm{q}}{2} + \frac{l_\mathrm{d}-l_\mathrm{q}}{2}\cos 2\delta & \frac{l_\mathrm{d}-l_\mathrm{q}}{2}\sin 2\delta \\ \frac{l_\mathrm{d}-l_\mathrm{q}}{2}\sin 2\delta & \frac{l_\mathrm{d}+l_\mathrm{q}}{2} - \frac{l_\mathrm{d}-l_\mathrm{q}}{2}\cos 2\delta \end{vmatrix} \tag{3}$$

From (1) through (3) the voltage equation becomes

$$\boldsymbol{u}_\mathrm{s}^{(\mathrm{S})} = r_\mathrm{s}\boldsymbol{i}_\mathrm{s}^{(\mathrm{S})} + \frac{d}{d\tau}\left(\boldsymbol{l}_\mathrm{s}^{(\mathrm{S})} * \boldsymbol{i}_\mathrm{s}^{(\mathrm{S})}\right) + \frac{d\boldsymbol{\psi}_\mathrm{sf}(\delta)^{(\mathrm{S})}}{d\tau}. \tag{4}$$

The rotor-fixed reference frame (superscript $^{(\mathrm{R})}$) is preferred for further analysis as it decouples the variables and simplifies the equations. The coordinate transformation leads to

$$\begin{aligned} \boldsymbol{\tau}_\mathrm{s} * \frac{d\boldsymbol{i}_\mathrm{s}^{(\mathrm{R})}}{d\tau} + \boldsymbol{i}_\mathrm{s}^{(\mathrm{R})} &= -\mathrm{j}\omega\, \boldsymbol{\tau}_\mathrm{s} * \boldsymbol{i}_\mathrm{s}^{(\mathrm{R})} \\ &- \frac{1}{r_\mathrm{s}}\left(\mathrm{j}\omega\boldsymbol{\psi}_\mathrm{sf}^{(\mathrm{R})} + \omega\frac{d\boldsymbol{\psi}_\mathrm{sf}(\delta)^{(\mathrm{R})}}{d\delta}\right) + \frac{1}{r_\mathrm{s}}\boldsymbol{u}_\mathrm{s}^{(\mathrm{R})} \end{aligned} \tag{5}$$

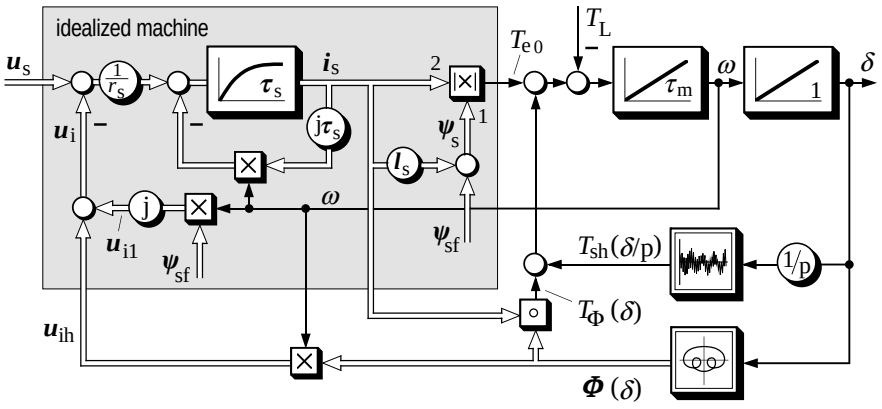

Fig. 1: Complex signal flow graph of a PM machine; *p*: number of polepairs

The voltage equation (5) is visualized by a complex first-order system [16] located in the shaded box of the signal flow graph Fig. 1. The feedback signal $-\mathrm{j}\omega\boldsymbol{\tau}_\mathrm{s} * \boldsymbol{i}_\mathrm{s}$ indicates that the stator winding rotates at the angular velocity $-\omega$ against the reference frame. The stator time constant is expressed by the tensor

$$\boldsymbol{\tau}_\mathrm{s} = \frac{1}{r_\mathrm{s}}\boldsymbol{l}_\mathrm{s}, \tag{6}$$

where

$$\boldsymbol{l}_\mathrm{s} = \boldsymbol{l}_\mathrm{s}^{(\mathrm{R})} = \begin{vmatrix} l_\mathrm{d} & 0 \\ 0 & l_\mathrm{q} \end{vmatrix} = \boldsymbol{C} * \boldsymbol{l}_\mathrm{s}(\delta)^{(\mathrm{S})} * \boldsymbol{C}^\mathrm{T} \tag{7}$$

is the tensor of the stator inductance in rotor coordinates. It is obtained by rotating (3) with the help of the transformation matrix

$$\boldsymbol{C}(\delta) = \begin{vmatrix} \cos\delta & \sin\delta \\ -\sin\delta & \cos\delta \end{vmatrix}, \tag{8}$$

which eliminates the dependency on the rotor position angle. The time constant of the stator winding as given in (6) exhibits a spatial orientation which models the saliency of the rotor. The resulting reluctance torque is independent of the rotor field; it is nonzero when both stator current components, i_d and i_q, are nonzero. The back-emf component which is induced at nonzero reluctance torque originates from the complex factor $\boldsymbol{\tau}_\mathrm{s}$ in the feedback term $-\mathrm{j}\omega\boldsymbol{\tau}_\mathrm{s} * \boldsymbol{i}_\mathrm{s}$ shown in the machine model Fig. 1.

The magnet induced back-emf in (5) is

$$\boldsymbol{u}_\mathrm{i} = \mathrm{j}\omega\boldsymbol{\psi}_\mathrm{sf}^{(\mathrm{R})} + \omega\frac{d\boldsymbol{\psi}_\mathrm{sf}(\delta)^{(\mathrm{R})}}{d\delta} = \boldsymbol{u}_\mathrm{i1} + \boldsymbol{u}_\mathrm{ih}\ . \tag{9}$$

Note that $\boldsymbol{u}_\mathrm{i}$ refers only to the magnet induced back-emf, for which the expression back-emf will be used. Subsequently, all equations will be referred to in rotor coordinates; the superscript $^{(\mathrm{R})}$ is then omitted for simplicity.

The first term in (9) is the fundamental back-emf component $\boldsymbol{u}_\mathrm{i1}$; it is aligned with the *q*-axis, and its magnitude is proportional to the angular velocity ω. The second term describes the variation of the flux linkage $\boldsymbol{\psi}_\mathrm{sf}$ with the rotor position angle δ. This variation is zero in rotor coordinates on condition that the spatial distribution of the permanent magnet flux linkage $\boldsymbol{\psi}_\mathrm{sf}$ is sinusoidal. In such a case, the flux linkage with the stator winding is independent of the rotor position δ: the space vector $\boldsymbol{\psi}_\mathrm{sf}^{(\mathrm{R})}$ is constant and has only a real component. Its derivative $d\boldsymbol{\psi}_\mathrm{sf}/d\tau = 0$.

In a real PM machine, the flux density distribution around the airgap is approximately rectangular. It is almost constant under the magnet poles, and close to zero in the gap between the poles. Special winding geometries can be used to establish a flux linkage with the stator that is sinusoidally distributed in space. Residual deviations from the sinusoidal distribution can be described by a flux linkage vector $\boldsymbol{\psi}_\mathrm{sf}(\delta)$ that,

being expressed in rotor coordinates, varies with the rotor position δ. Such variations define the complex function of the flux linkage harmonics

$$\boldsymbol{\Phi}(\delta) = \frac{d\boldsymbol{\psi}_{\mathrm{sf}}(\delta)}{d\delta}. \tag{10}$$

A comparison with (9) shows that, at rated speed, this function is formally identical with the space vector $\boldsymbol{u}_{\mathrm{ih}}$ of the back-emf harmonics in the stator winding:

$$\boldsymbol{\Phi}(\delta) = \frac{\boldsymbol{u}_{\mathrm{ih}}(\delta)}{\omega}. \tag{11}$$

Its trajectory in rotor coordinates was computed from a measurement in the no-load generator mode of the rotor induced harmonic voltage and of speed. An 8-pole PM machine was used, the data of which are given in the Appendix. The trajectory in Fig. 2 is periodic with 360° electric, being detailed in Fig. 2(a) and Fig. 2(b) for 0 – 180° and 180° – 360°, respectively. For comparison, the two-axes components of the back-emf vector (9) are oscillographed in Fig. 2(c).

It is important to note that, owing to the presence of flux linkage harmonics, field coordinates and rotor coordinates do not coincide in this type of synchronous machine.

The Fourier spectrum Fig. 2(d) of the complete trajectory represented by Fig. 2(a) and Fig. 2(b) shows that space harmonics of 2nd and 6th order are predominant. Harmonics of higher order than 12 tend to be small, and their contribution to torque ripple can be neglected. The existence of even harmonics indicates the presence of a zero sequence system in the back-emf trajectory, while components having a negative sign relate to flux linkage harmonics of counter-clockwise rotation.

The electromagnetic torque generated by the fundamental distributions is expressed by

$$T_{\mathrm{e0}} = |\boldsymbol{\psi}_{\mathrm{s}} \times \boldsymbol{i}_{\mathrm{s}}| = \left|\left(\boldsymbol{l}_{\mathrm{s}} * \boldsymbol{i}_{\mathrm{s}} + \boldsymbol{\psi}_{\mathrm{sf}}\right) \times \boldsymbol{i}_{\mathrm{s}}\right|, \tag{12}$$

where $\boldsymbol{\psi}_{\mathrm{sf}}$ is substituted from (2). In (12), the reluctance torque is represented by $(\boldsymbol{l}_{\mathrm{s}} * \boldsymbol{i}_{\mathrm{s}}) \times \boldsymbol{i}_{\mathrm{s}}$.

Since the space vector approach cannot represent spatial distributions other than sinusoidal, the space harmonics of the flux linkage distribution $\boldsymbol{\psi}_{\mathrm{sf}}(\delta)$ are expressed in the time domain. Their effect is represented by the back-emf term $\boldsymbol{u}_{\mathrm{ih}}(\tau)$, which is then time-varying also in rotor coordinates. The torque contribution of the flux linkage harmonics is derived from the equivalence of electrical and mechanical power

$$T_{\Phi}(\delta) = \frac{1}{\omega}\boldsymbol{u}_{\mathrm{ih}}(\tau) \circ \boldsymbol{i}_{\mathrm{s}} = \boldsymbol{\Phi}(\delta) \circ \boldsymbol{i}_{\mathrm{s}}. \tag{13}$$

This equation holds regardless of whether the internal distributions of voltages, currents and flux linkages are sinusoidal or not.

The mechanical system is described by the equations of motion

$$\frac{d\omega}{d\tau} = \frac{1}{\tau_{\mathrm{m}}}\left[T_{\mathrm{e0}}(\tau) + T_{\Phi}(\delta) + T_{\mathrm{sh}}(\delta) - T_{\mathrm{L}}(\delta)\right] \tag{14}$$

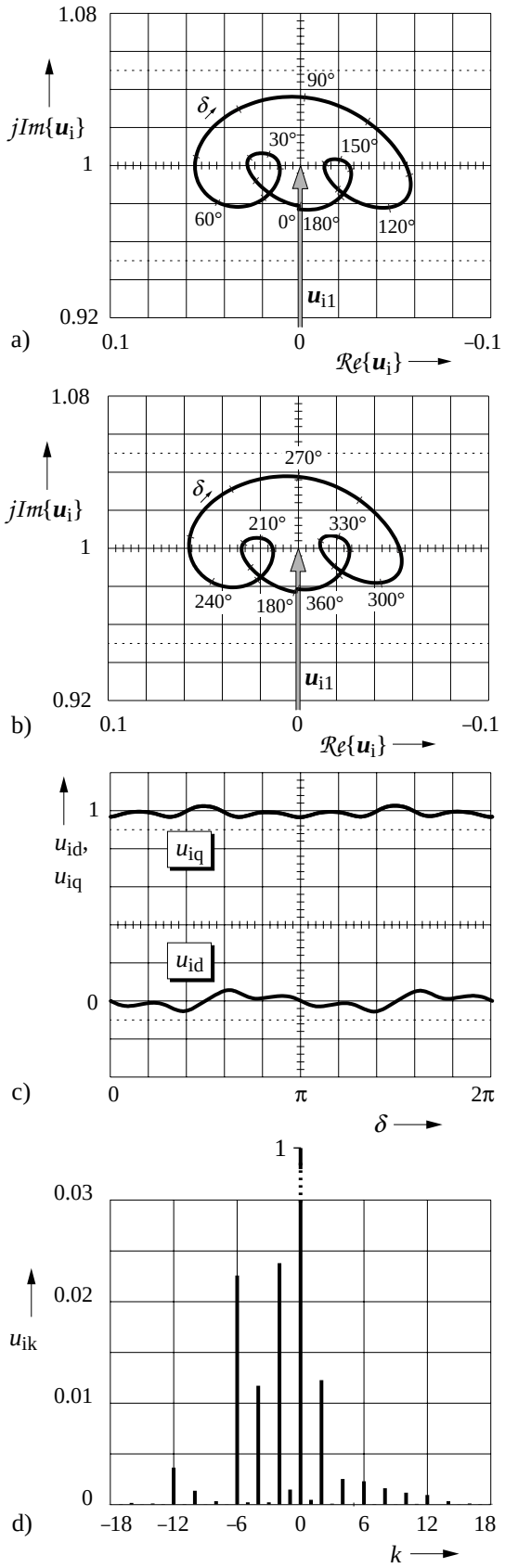

Fig. 2: Effects of nonsinusoidal stator flux distribution; (a) and (b) complex function $\boldsymbol{\Phi}(\delta)$ of the flux linkage harmonics, (c) two-axes components of the complex function $\boldsymbol{\Phi}(\delta)$ in rotor coordinates, (d) harmonic spectrum of $\boldsymbol{\Phi}(\delta)$ in rotor coordinates

$$\frac{d\delta}{d\tau} = \omega\,, \tag{15}$$

where τ_m is the normalized mechanical time constant, T_{e0} is the fundamental electromagnetic torque, T_Φ is the harmonic torque caused by nonsinusoidal flux linkage distribution, T_{sh} is the torque due to stator slotting and rotor eccentricity (cogging torque), and T_L is the load torque. In (14), the fundamental electromagnetic torque T_{e0} is a function of the time dependent state variables in (12); the harmonic torque components T_Φ and T_{sh} depend on the rotor angle. Note that the rotor angle δ is expressed in terms of electrical radians. The same applies to the angular velocity ω of the rotor.

Equations (12), (14) and (15) are represented on the upper right-hand side of the signal flow diagram Fig. 1. The sources of torque ripple are visualized by the two nonlinear functions below. The scalar function $T_{sh}(\delta/p)$ represents the stator slot and eccentricity effects. Its argument is δ/p, where p is the number of pole pairs. The argument takes into account that the rotor angle δ of the machine model refers to an equivalent 2-pole machine, while the eccentricity effects in the real machine repeat every full revolution of the rotor.

The complex function $\boldsymbol{\Phi}(\delta)$ of the flux linkage harmonics models the effect of an existing nonsinusoidal flux linkage according to (11) and (13). It relies on the space vector $\boldsymbol{u}_{ih}(\tau)$ of the back-emf, which, in fact, symbolizes a sinusoidal distribution in space [16, 17]. Although such distribution does not exist in this machine, the representation (13) of the harmonic torque is nevertheless correct, since the nonsinusoidal spatial distribution $\omega\,\boldsymbol{\Phi}(\delta)$ from (11) has the same effect on the machine as the sinusoidal distribution $\boldsymbol{u}_{ih}$.

5. The Current Control System

A very-high bandwidth current control system was designed for high-frequency torque ripple compensation. It comprises a dynamic feedforward structure for decoupled torque control, an error prediction scheme, and a deadbeat current controller [18]. The parameters of the current predictor and the deadbeat controller must be accurately set. An automated self-commissioning scheme is provided for this purpose. The deadbeat controller eliminates the current error within one subcycle of the pulsewidth modulator (e. g. 25 µs at 20 kHz switching frequency). The inherent sampling delay of digital signal processing does not limit the effective bandwith since the compensation functions are fully predictable. An underlying space vector modulator ensures low time harmonics and, having a reference voltage input $\boldsymbol{u}^*$, favors self-commissioning.

The current control system forms part of the torque ripple compensation scheme Fig. 9. Its performance is demonstrated in Fig. 3 in comparison with a PI current controller plus feedforward decoupling of the machine dynamics.

6. Self-Commissioning Scheme

The proposed torque harmonics suppression scheme and the associated deadbeat current control system require the accurate knowledge of the following machine properties:

- stator resistance r_s,
- stator inductances l_d and l_q,
- the complex function $\boldsymbol{\Phi}(\delta)$ of the flux linkage harmonics,
- the function $T_{sh}(\delta)$ of the slot harmonic torque.

Usually these data are not, or only partially, included in the data sheet of the machine. Particularly the harmonic flux linkage characteristic $\boldsymbol{\Phi}(\delta)$ differs with every individual machine, making the commissioning of such drive system a very complicated task. Therefore, a self-commissioning scheme is indispensable. It automatically determines the correct parameter settings, and the specific functions that characterize the torque harmonics. As the permanent magnet properties vary with temperature, and may also change following a current overload situation, an on-line adaptation scheme for the flux linkage harmonics is required. At best, such identification schemes should work without hardware additions to an existing control system. This constraint is important for applications in an industrial environment.

A self-commissioning scheme as specified before is described next. It relies only on the name-plate data of the machine, which is entered by the operator through a user interface. The following name-plate data are required: rated current, rated speed and the number of poles. In the case considered here, the motor is a Mavilor Discodyn ac servomotor type SE 808 which is already designed for minimum torque ripple. Its cross-section is shown in Fig. 4.

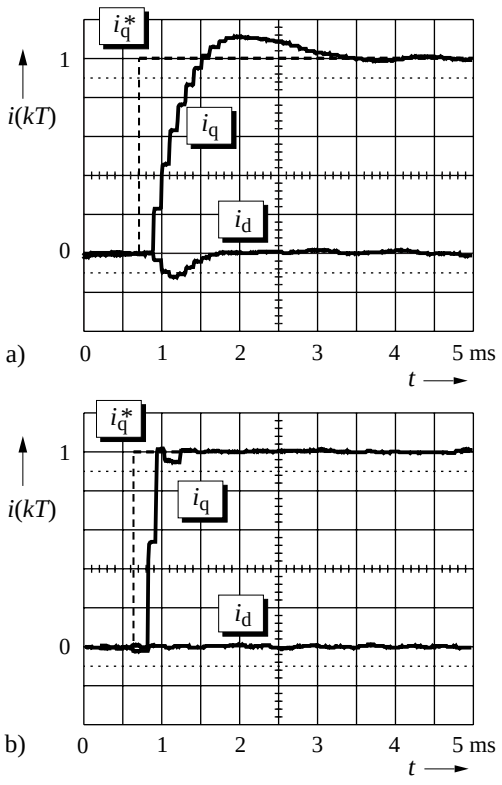

Fig. 3: Comparison of current controllers, (a) PI-controller with feedforward decoupling, (b) deadbeat controller; sampling frequency 10 kHz

6.1 Measurement of the stator resistance

When the automated identification process is started, the stator resistance is measured first. The pulsewidth modulator receives an input signal $\boldsymbol{u}^*$ such that a voltage vector of arbitrary, but constant phase angle is applied to the machine. On condition that the variable inverter switching delay is accurately compensated [5], the average stator voltage being applied to the machine equals the reference voltage vector. During the test, the magnitude of the applied voltage vector is started at a minimal value and then increased slowly until the rated current flows in the stator windings. The stator resistance is then taken as the ratio between the reference voltage and the measured current. Irregularities of the pulsewidth modulator and the inverter are compensated by repeating the measurement at different phase angles of the voltage vector. The obtained results are averaged. The measurement error with this method is less than 5%. Such accuracy is more than sufficient as the stator resistance is not a critical parameter in the proposed control scheme. The error due to its thermal variations is much higher.

6.2 Identification of the stator inductance

The measurement of the stator resistance terminates with the machine carrying a dc stator current of about rated magnitude. The current is maintained stationary for an adequate duration of time so as to permit the rotor to align with the stator field. The stator current then becomes the *d*-axis current.

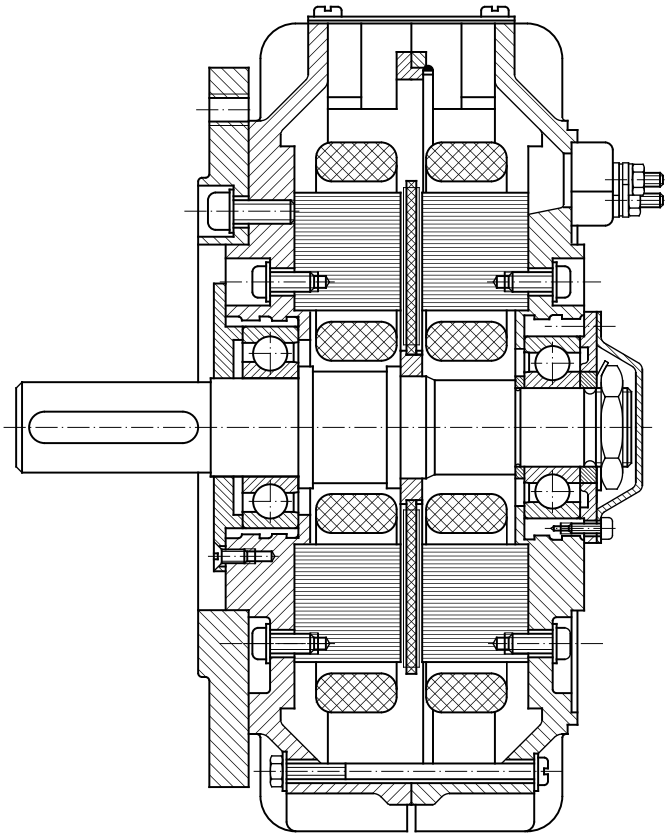

Fig. 4: Mechanical construction of the Mavilor Discodyn ac servomotor SE 808

The saliency of the machine produces a reluctance torque component that tends to deviate the rotor from that angular position which is determined by the stator current space vector, even at zero shaft torque. The reluctance torque was found negligible in our laboratory machine, and hence no further measures were taken. If necessary, however, the deviation of the rotor position due to the reluctance torque could be determined by tuning the average imaginary component of the measured back-emf vector (Fig. 7) to zero. This would require an additional test at nonzero speed.

In the identification process, the phase angle of the stator current space vector is now set to $arg(\boldsymbol{i}_s) \approx 30°$. The reason for selecting this particular angular position is that the pulsewidth modulator works more accurately if its reference vector is located half way between two active switching state vectors. The error introduced by the minimum on-time condition of the inverter is then minimum, and $\boldsymbol{u}_s = \boldsymbol{u}^*$.

After the alignment of the rotor to a defined position, the modulator is turned off, and the machine deenergizes.

A constant voltage vector, having the same phase angle as in the previous test, is now applied to the stator winding. Its predetermined magnitude is controlled by pulsewidth modulation. To reduce the magnitude error of the pulsewidth modulation process, the voltage amplitude is selected high. The stator current builds up exclusively in the *d*-axis, rising exponentially according to

$$\boldsymbol{i}_d = \frac{\boldsymbol{u}^*}{r_s}\left(1 - exp\left(-\frac{r_s}{l_d}\tau\right)\right), \qquad (16)$$

from which equation the *d*-axis inductance l_d can be determined. Fig. 5(a) shows the *d*-axis response in terms of those current components i_α and i_β in stator coordinates that are acquired by the system. The stator current (16) is sampled at those time instants at which its harmonic component equals zero. The sampling instants kT_s are determined by the pulsewidth modulator [4]; they are marked by the rising edges of the clock signal in the lower trace of Fig. 5(a). T_s is the sampling period.

Fig. 5(b) shows the *q*-axis response, from which l_q is determined. The oscillogram was recorded in the same way as in the previous test, but with the voltage reference vector advanced by 90°. To demonstrate the influence of saturation, the current slopes in Fig. 5 were arbitrarily increased and the currents driven beyond their rated value. While the *q*-axis inductance appears fairly linear, saturation in the *d*-axis becomes visible at $i_s > 2\ i_{sR}$, where i_{sR} is the rated stator current.

The exponential characteristic of the response is barely visible in Fig. 5 since the stator time constant is much larger than the interval of measurement. This circumstance favourably permits measuring the *q*-axis inductance by recording the step response of the *q*-axis current before the electromagnetic torque produced by this current component accelerates the rotor appreciably. This also ensures that the back-emf remains near zero, and its influence on the current need not be considered.

The stator inductance values l_d and l_q are calculated from *n* discrete samples $\boldsymbol{i}_s^{(S)}(kT)$, $k \in [1, n]$, of the stator current. A total number of $n = 8$ current samples proved to be

sufficient for an accurate evaluation of the inductance. They are transformed to rotor coordinates, and a table containing the values

$$y_k = 1 - \frac{r_s}{u^*} i_{d,q}(kT) = exp\left(-\frac{r_s}{l_{d,q}} kT\right), \quad k \in [1,8] \tag{17}$$

is established. The stator inductances l_d and l_q are then obtained by exponential regression:

$$l_{d,q} = -r_s \frac{n\sum_{k=1}^{n}(kT)^2 - \left(\sum_{k=1}^{n} kT\right)^2}{n\sum_{k=1}^{n} kT \ ln y_k - \sum_{k=1}^{n} kT \sum_{k=1}^{n} ln y_k}, \quad k \in [1,8] \tag{18}$$

6.3 Identification of the mechanical time constant

The identified values of r_s, l_d and l_q permit adjusting the parameters of regular PI current controllers for the *d*- and *q*-axis currents. The controllers are then used to inject a *q*-axis current step of rated magnitude into the machine, producing unity torque, $T_{eR} = 1$. The acceleration $\Delta\omega/\Delta t$ of the drive system is measured, and the mechanical time constant is obtained from

$$\tau_m = T_{eR} \frac{\Delta\tau}{\Delta\omega}. \tag{19}$$

This value is used to set the parameters of the speed controller.

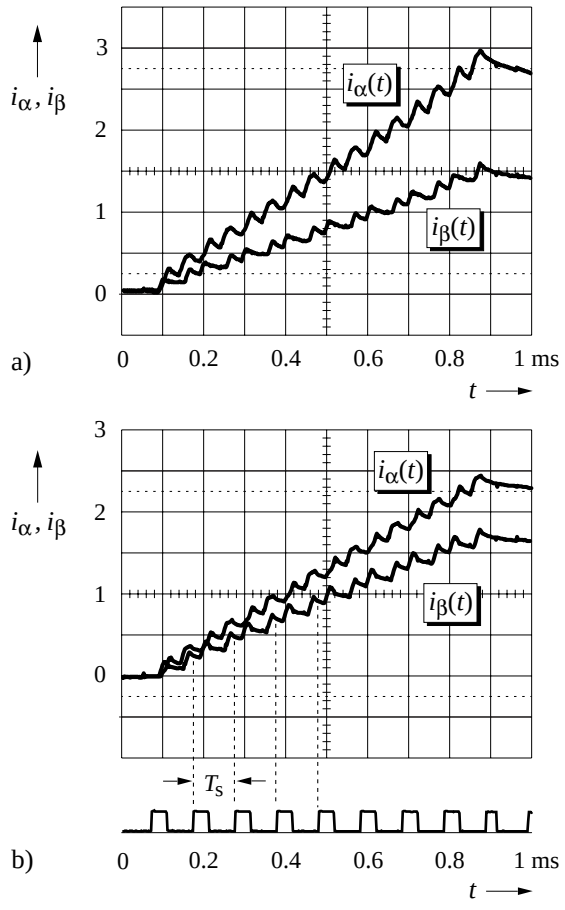

Fig. 5: Identification of the stator inductances following a voltage step input, (a) *d*-axis response, (b) *q*-axis response, lower trace: sampling signal

6.4 Identification of the flux linkage harmonics

The effect of flux linkage harmonics is acquired in an on-line process during normal operation of the drive system, thus permitting the adaptation of torque ripple compensation to the prevailing conditions. The flux linkage harmonics are reflected in the distortion of the back-emf, (9) and (5),

$$\boldsymbol{u}_i = \boldsymbol{u}_s - r_s \boldsymbol{i}_s - \boldsymbol{l}_s * \frac{d\boldsymbol{i}_s}{d\tau} - j\omega \boldsymbol{l}_s * \boldsymbol{i}_s, \tag{20a}$$

where

$$\omega = \frac{d\delta}{d\tau}. \tag{20b}$$

Hence the flux linkage harmonics can be extracted from this waveform as a function of the rotor position angle *d*. The machine parameters r_s and $\boldsymbol{l}_s$ in (20) are known from the initial self-commissioning tests. The stator voltage $\boldsymbol{u}_s$ is a switched quantity and equals zero when the zero vector is on. Evaluating (20) during this time interval avoids the measurement of $\boldsymbol{u}_s$. However, a problem is associated with the evaluation of the current derivative $d\boldsymbol{i}_s/dt$. The numerical differentiation is bound to be inaccurate in the presence of noise.

To improve on this, all terms in (20) are averaged over a switching subcycle of the pulsewidth modulator. The integration of (20) leads to:

$$\int_{T_s} \boldsymbol{u}_i dt = \int_{T_s} \boldsymbol{u}_s dt - \int_{T_s} r_s \boldsymbol{i}_s \, dt - \int_{T_s} \boldsymbol{l}_s * \frac{d\boldsymbol{i}}{dt} dt - \int_{T_s} j\omega \boldsymbol{l}_s * \boldsymbol{i} \, dt \tag{21a}$$

$$\int_{T_s} \omega \, dt = \int_{T_s} \boldsymbol{l}_s \frac{d\delta}{dt} dt \tag{21b}$$

where T_s is the subcycle interval. Its short duration of 50 μs or less supports the following assumptions:

- The back-emf changes linearly.
- The average output voltage $\bar{\boldsymbol{u}}_s$ equals the reference voltage vector $\boldsymbol{u}^*$.
- The stator current derivative is constant. Hence the average stator current equals the average of the two current samples at the beginning and the end of the subcycle interval.
- The angular velocity ω of the rotor is constant.

Using these conditions we have from (21)

$$\bar{\boldsymbol{u}}_i\left(\frac{\delta_k + \delta_{k-1}}{2}\right) = \boldsymbol{u}^*_{k-1} - r_s \bar{\boldsymbol{i}}_k - \boldsymbol{l}_s * \frac{\boldsymbol{i}_k - \boldsymbol{i}_{k-1}}{T_s} - j\bar{\omega} \boldsymbol{l}_s * \bar{\boldsymbol{i}}_k \tag{22a}$$

where $$\bar{\boldsymbol{i}}_k = \frac{1}{2}(\boldsymbol{i}_k + \boldsymbol{i}_{k-1}), \tag{22b}$$

an $$\bar{\omega} = \frac{\delta_k - \delta_{k-1}}{T_s}. \tag{22c}$$

The relationship in (22) between the sampled and calculated data is displayed in Fig. 6. Note that only current and speed samples are taken, as in noß˜al operation. All variables are referred to in rotor coordinates.

Equation (22) is continuously evaluated during operation to be adapted to the actual magnetic properties of the machine. The acquired data are used to compute the flux linkage harmonics from (9) and (11). The result is exemplified in Fig. 7(a). The remaining distortions are due to quantization effects, particularly of the pulsewidth modulator. They are eliminated by a nonrecursive filter (FIR-filter) of constant group velocity, defined by

$$\boldsymbol{\Phi}(k) = \sum_{i=-N}^{N} \alpha_i \, \boldsymbol{\Phi}^{(\mathrm{D})}(k-i), \qquad i \in [1,8], \tag{23}$$

where $\boldsymbol{\Phi}(\delta)^{(\mathrm{D})}$ represents the distorted preliminary data. The values of the filter coefficients α_{i} are calculated using the Hamming window function:

$$\alpha_i = \alpha_{-i} = \frac{\sum_{i=-N}^{N} \alpha_i}{2N+1} \frac{\sin \frac{2\pi f_{\mathrm{c}} i}{k_{\max}}}{i\pi} \cdot \left(0.54 - 0.46 \cos\left(\frac{i+1}{N}\pi\right)\right), \quad i \in [0, N] \tag{24}$$

Here, $k_{\max} = 2048$ is the number of samples taken per pole pair, and f_{c} is the cut-off frequency of the filter, which is set to the 13th harmonic at rated speed (2600 Hz). The smoothened flux linkage function $\boldsymbol{\Phi}(\delta)$ is shown in Fig. 7(b). The same function, but measured off-line on a machine test bench is shown for comparison. The curves in Fig. 7 were obtained on-line from zero initial values after three minutes of operation including noise reduction as described by (24).

6.5 Identification of slot harmonics

The slot harmonic torque function $T_{\mathrm{sh}}(\delta)$ is indirectly acquired by operating the machine at very low speed. The torque harmonic frequency is then also very low and well within the bandwidth of the speed control loop. Hence the torque ripple is instantaneously compensated by the speed controller in its effort to maintain the speed constant. The slot harmonic function $T_{\mathrm{sh}}(\delta)$ can be extracted from the torque producing current $i_{\mathrm{q}}(\delta)$, which is sampled and stored in a table. For simplicity, $i_{\mathrm{d}} = 0$.

Readings are taken over more than one full revolution of the motor shaft with a view to remove statistical noise from the sampled data. Following the first revolution, the readings taken during the ensuing k revolutions are used to modify the table according to

$$i_{\mathrm{q}}(\delta, \mathrm{k}) \Leftarrow \frac{i_{\mathrm{q}}(\delta, \mathrm{k}-1) + g \cdot i_{\mathrm{q}}(\delta, \mathrm{k})}{1+g}. \tag{25}$$

The weight factor g is selected in a compromise to obtain a smooth curve in minimum time. A value of $g = 1.55$ worked well. The resulting waveform is shown in Fig. 8(a). This curve represents the total machine torque. Its ac content is the torque ripple, and the dc offset is the load torque including friction of the motor bearings. Hence

$$T_{\mathrm{sh}}(\delta) = i_{\mathrm{q}}(\delta) \cdot \mathit{Im}\{\boldsymbol{\Phi}(\delta)\} - \int_0^{2\pi} i_{\mathrm{q}}(\delta) d\delta \tag{26}$$

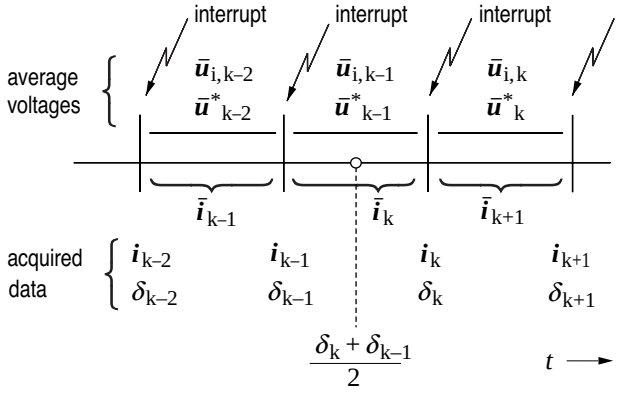

Fig. 6: Timing diagram; the k-values number the sampling instants

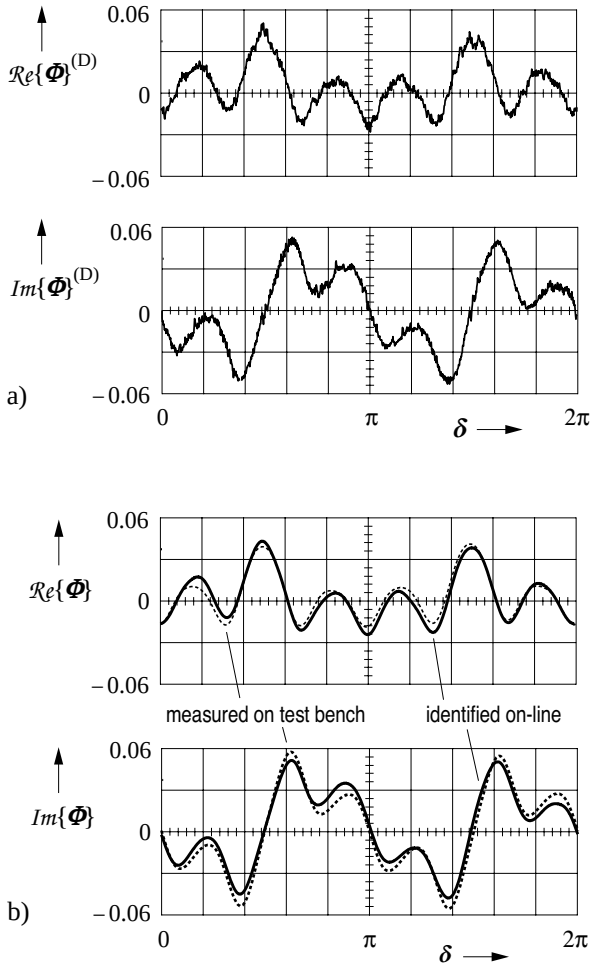

Fig. 7: Components of the rotor induced back-emf; (a) measured waveform after transformation to rotor coordinates, superscript (D) indicates distorted function; (b) rotor induced back-emf after nonrecursive filtering, compared with the accurate waveform obtained off-line on a test bench

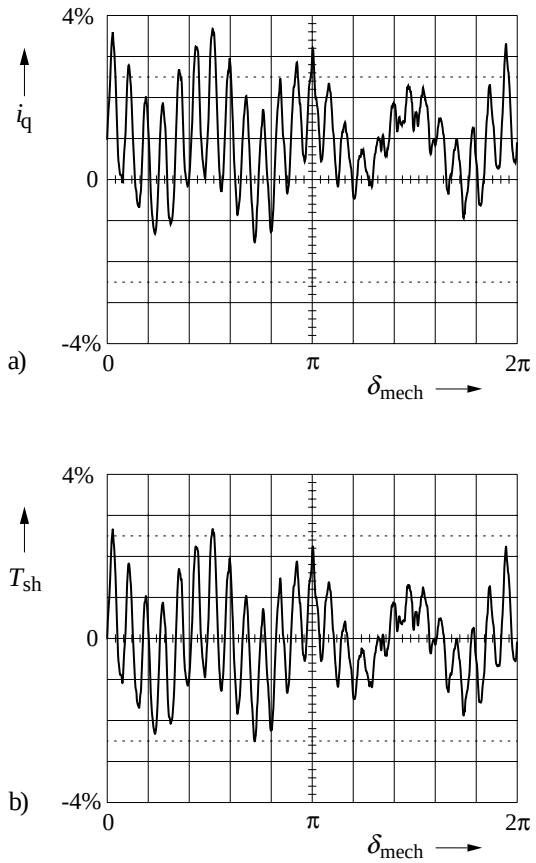

Fig. 8: Identification of slot harmonic torque, (a) *q*-axis current versus rotor position angle, (b) extracted slot harmonics

is the normalized slot harmonic torque. The factor $\mathit{Im}\{\boldsymbol{\Phi}(\delta)\}$ in (26) eliminates the flux linkage harmonics at $\boldsymbol{i}_d = 0$, which is derived from (9), (11) and (12).

Fig. 8(b) shows the torque ripple resulting from slot harmonics as extracted from an 8-pole sinusoidal PM machine using (26). There are 23 pulsations visible per rotor revolution which relate to the slot effect. The additional low-frequency component results from different pole flux levels of the four pole pairs, possibly combined with rotor eccentricity. The latter effect may also account for the varying amplitude of the slot ripple function. The peak ripple amplitude amounts to 2.5% of rated torque. Note that this method of acquiring the slot harmonics inherently includes any periodic torque ripple of the mechanical load in the recorded data, which will then be compensated as well.

Given the low speed of operation during this test, the second term in (26) represents basically Coulomb friction as generated by the machine and the load. The Coulomb friction torque reverses sign at speed reversal, thus introducing an instantaneous disturbance. During normal operation, the disturbance is compensated using the identified friction torque.

7. Harmonic Torque Compensation

The identified torque ripple functions are used for compensating the imperfections of the drive motor. Fig. 9 shows the signal flow diagram of the compensation scheme. The shaded block contains the current control system. The *d*-axis reference $i_d^* = 0$, and hence the reluctance torque $(\boldsymbol{l}_s^* \boldsymbol{i}_s) \times \boldsymbol{i}_s = 0$, which term is contained in (12); The reluctance torque would be small anyway even if $i_d = 0$ since $l_d \approx l_q$. The *q*-axis reference i_q^* controls the torque and hence is derived from the speed controller. The additional signal $i_{q\,comp} = i_{q\,sh} + i_{q\Phi}$ compensates the slot harmonics, and the flux linkage harmonics, respectively. The compensation signals are read from two tables, one being addressed by the mechanical rotor position angle, and the other by the electrical rotor position angle.

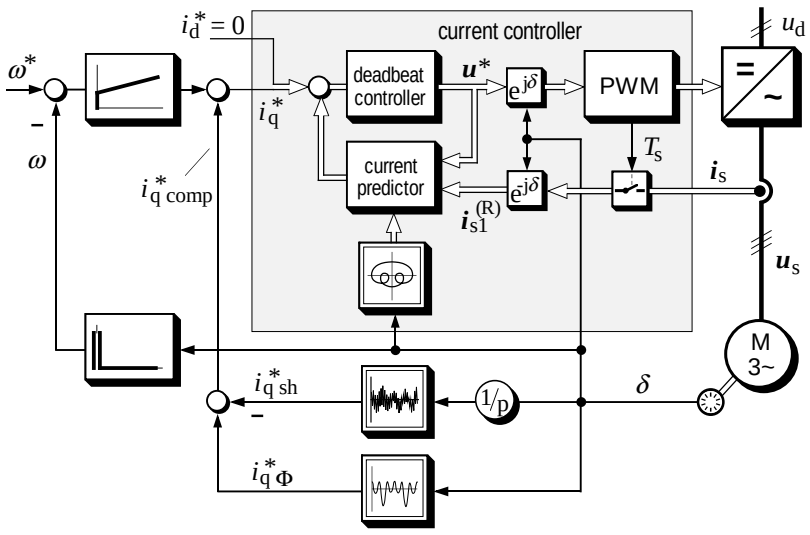

Fig. 9: Signal flow diagram of the speed and torque control system (δ in degrees electrical)

Fig. 10 shows the steady-state stator current trajectory including the compensation current for torque harmonics. Four different patterns exist for an 8-pole machine, demonstrating that the compensation function repeats every mechanical revolution.

The effect of slot harmonics compensation on the rotor speed is demonstrated in Fig. 11(a). This oscillogram was recorded at no-load to eliminate the influence of flux linkage harmonics. The resolution of speed measurement is $4 \cdot 10^{-6}$.

The compensation of flux linkage harmonics is demonstrated in Fig. 11(b) with rated torque applied to the motor shaft. The slot harmonic torque compensation was enabled throughout this measurement, which separates the slot effect. A water cooled, torque controlled iron-powder brake was used for this test to ensure that the ripple torque added by the load is minimum. A dc machine proved to be inadequate for this purpose. Some of the residual speed ripple which is seen in Fig.

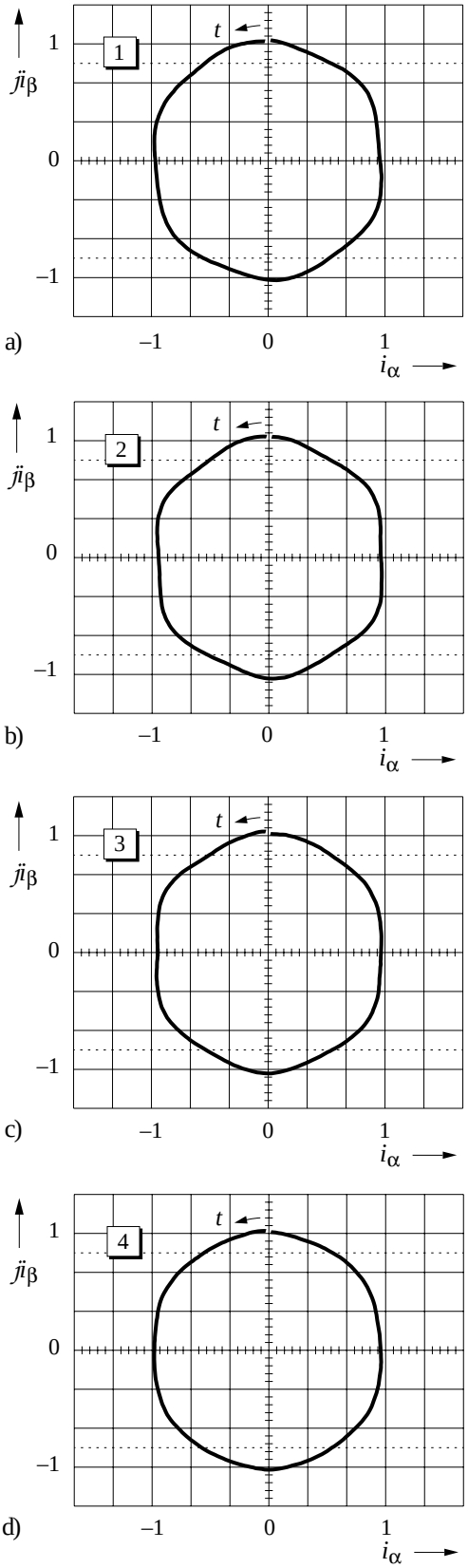

Fig 10: Recorded stator current trajectories at steady-state, compensation of flux linkage harmonics. Each trajectory relates to a quarter revolution of the 8-pole machine

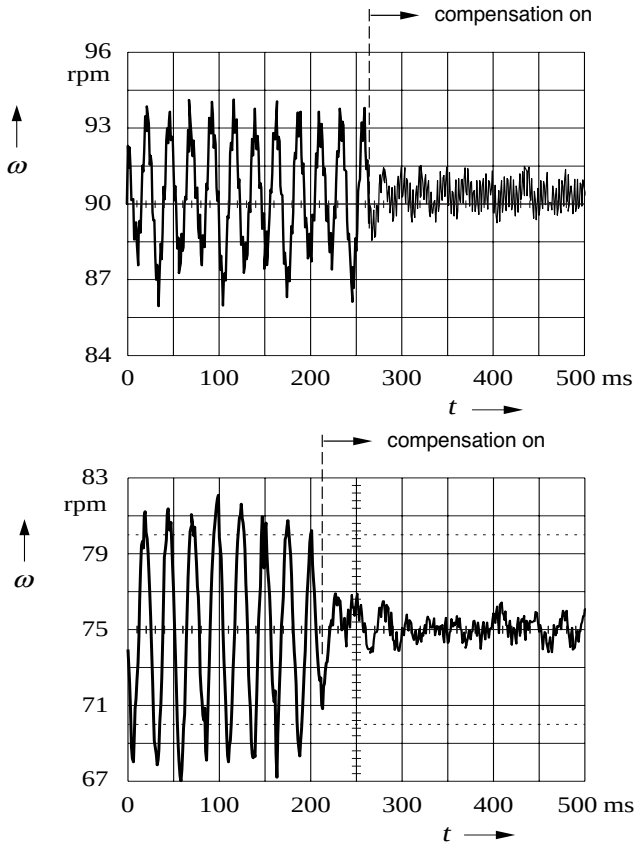

Fig. 11: Effect harmonic compensation; (a) compensation of slot harmonics, (b) compensation of flux linkage harmonics.

11 with the compensation activated could be contributed by the load.

To demonstrate the performance of the current control system, the electromagnetic torque of the machine was estimated from terminal quantities. The estimated torque comprises flux linkage harmonics, but excludes slot harmonics. PI-controllers fail to suppress the torque harmonics due to their limited bandwidth and sampling delay effects. These lead to instabilities which amplify the torque ripple, when given the task to compensate the flux linkage harmonics. The performance of the PI-controller is shown in Fig. 12(a). The deadbeat controller performs much better owing to its higher bandwidth. This is demonstrated in Fig. 12(b).

The estimated electromagnetic torque without ripple compensation is shown in Fig. 12(c) for comparison. This oscillogram was recorded while forcing pure sinusoidal stator currents by deadbeat current control. Operating at forced sinusoidal stator voltages basically reproduces the back-emf waveform Fig. 7 as a harmonic torque waveform.

Note that the motor used for the experiments is an inherently smooth machine, designed for minimum torque ripple.

8. Practical Implementation

A standard 80C166 microcontroller system was used for the implementation in hardware. A 64-kB EPROM is provided to store the object code. The on-chip CAPCOM unit and A/D converters were used for PWM pattern generation

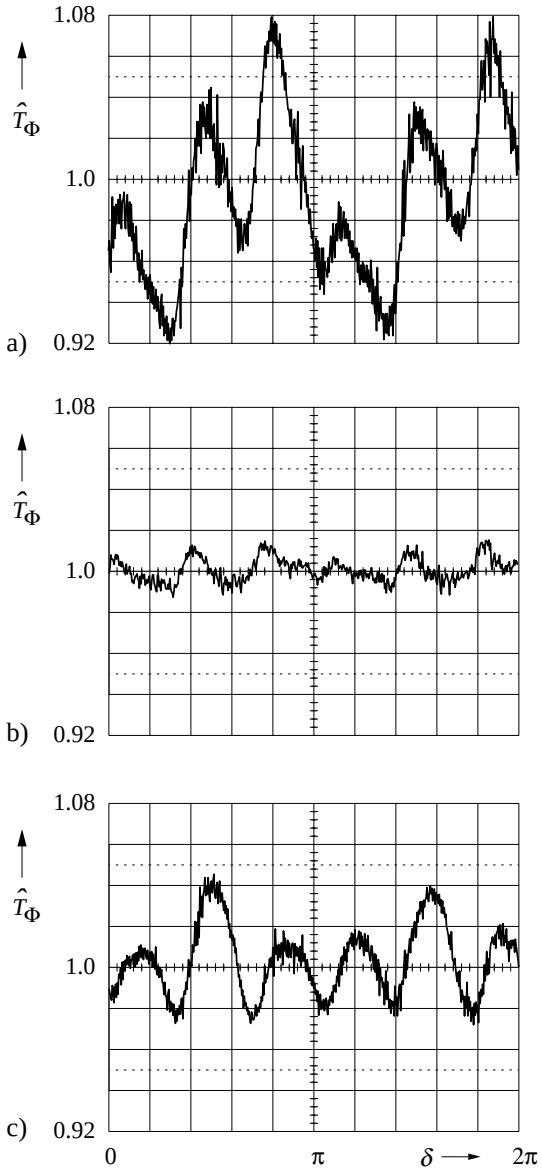

Fig. 12: Estimated machine torque at rated speed (slot ripple not included) with compensation of flux linkage harmonics, (a) PI current controller and feedforward decoupling scheme, (b) deadbeat current controller, (c) without compensation

and feedback signal conversion. Pulsewidth modulation was programmed in software. The sampling rate for current control was set to 10 kHz, a hardware limit for the response time of the current control loop. A higher bandwidth can be obtained using a DSP system.

9. Summary

Residual torque pulsations in PM synchronous machines of the sinusoidal flux linkage type impair their performance in critical applications. Torque pulsations are generated by deviations from the sinusoidal flux linkage distribution, and by stator slotting effects, unbalanced magnetization, and secondary phenomena. The critical ripple frequencies range up to 2 kHz.

The design of a fast ripple compensation scheme is based on a model of the parasitic effects, for which the complex state-variable approach is used. Its restricted validity, which extends only to sinusoidal distributions in space, is overcome by expressing space harmonic effects in the time domain. An automated self-commissioning scheme extracts the pertinent fundamental and harmonic parameters from the drive system. This is indispensable, since even machines from the same production batch may exhibit major differences. Variations of the back-emf due to varying magnet properties are continuously adapted during normal operation. High-bandwidth ripple compensation is enabled using a deadbeat current controller and current predictor. The underlying space vector modulator facilitates data acquisition without additional hardware and ensures low time harmonics. The inherent sampling delay of digital signal processing does not limit the effective bandwidth, since the harmonic compensation functions are fully predictable.

10. Nomenclature

$\boldsymbol{u}_\mathrm{s}$	stator voltage vector
$\boldsymbol{\psi}_\mathrm{sf}$	stator flux linkage produced by
$\boldsymbol{i}_\mathrm{s}$	stator current vector
	permanent magnets
r_s	winding resistance
$\boldsymbol{l}_\mathrm{s}$	stator inductance tensor
$\boldsymbol{\psi}_\mathrm{s}$	stator flux linkage vector
l_d, l_q	*d*-axis and *q*-axis inductance
τ	normalized time
δ	angular rotor position
ω_sR	nominal stator frequency
τ_s	stator time constant
$\boldsymbol{u}_\mathrm{i}$	back-emf vector
T_e0	electromagnetic torque excluding
$\boldsymbol{u}_\mathrm{i1}$	fundamental of back-emf vector
	harmonics
$\boldsymbol{\Phi}$	normalized flux linkage harmonics
T_eR	rated torque
τ_m	mechanical time constant
T_Φ	flux linkage harmonic torque
p	number of pole pairs
T_sh	slot harmonic torque
$\boldsymbol{u}_\mathrm{ih}$	vector of back-emf harmonics
T_L	load torque
α_i	filter coefficients of FIR filter
$\boldsymbol{u}^*$	reference voltage vector
f_c	cut-off frequency
T_s	sampling time

11. Appendix

The experiments described in this paper where carried out using the following PM machine:

rated power	1700 W
number of poles	8
rated speed	3000 rpm
max. speed	6000 rpm
rated current	6.8 A
max. current	64 A

rated torque @100˚ C	5.6 Nm
max. torque	52 Nm
rated back-emf	148 V
stator resistance	0.9 Ohm
d-axis inductance	3.1 mH
q-axis inductance	3.4 mH
number of rotor slots	23

12. References

1. T. M. Jahns, "Motion Control with Permanent-Magnet AC Machines", *Proceedings of the IEEE*, Vol. 82, No. 8, Aug. 1994, pp. 1241-1252.
2. M. Lajoie-Mazene, R. Carlson, J. C. Fagundes, "Analysis of Torque Ripple due to Phase Commutation in Brushless DC Machines", *IEEE Ind. Appl. Soc. Ann. Meet.*, Seattle, 1990, pp. 287-292.
3. J. Cros et al, "A Novel Current Control Strategy in Trapezoidal EMF Actuators to Minimize Torque Ripples due to Phase Commutation", *EPE European Conf. on Power Electronics and Applications (EPE)*, Brighton UK, 1993, Vol. 4, pp. 266-271.
4. J. Holtz, "Pulsewidth Modulation – A Survey". *IEEE Transactions on Industrial Electronics*, Oct. 1992, Vol. 39, No. 5, pp. 410-420.
5. Y. Murai, T. Watanabe, H. Iwasaki: Waveform Distortion Correction Circuit for PWM Inverters with Switching Lag-Times. *IEEE Transactions on Industry Applications*, Vol. 23, No.5, 1987, pp. 881-886.
6. Kempkes, "Improvement and Assessment of Parasitic Speed Variations in High-Precision Permanent Magnet Synchronous Motors" (in German), Ph.-D. Thesis, Aachen, 1991.
7. Marinescu, "Influence of Magnet Pole Size and Airgap Dimensions on Torque Ripple in Permanent Magnet Synchronous Machines" (in German),etz-Archiv, Vol. 10, No. 3, 1988, pp. 83-88.
8. H. Grotstollen, "Suppression of Torque Harmonics in Synchronous Motors by Injected Current Harmonics", *Archiv für Elektrotechnik*, Vol. 67, 1984, pp. 17-27.
9. H. Le Huy, R. Perret, R. Feuillet: "Minimization of Torque Ripple in Brushless DC Motor Drives", *IEEE Ind. Appl. Soc. Ann. Meet.*, Toronto, 1985, pp. 790-797.
10. E. Favre, L. Cardoletti, M. Jufer: "Permanent-Magnet Synchronous Motors: A Comprehensive Approach to Cogging Torque Suppression", *IEEE Trans. on Ind. Appl.*, Vol. 29, No. 6, Nov/Dec 1993, pp. 1141-1149.
11. Le-Huy, "Torque Characteristics of Brushless DC Motors with Imposed Current Waveforms", *IEEE Ind. Appl. Soc. Ann. Meeting*, Denver, 1986, pp. 176-181.
12. Amrhein, "Motor – Electronic Control – Precision of Rotation: Contributions for the Design of Permanent Magnet Excited Drive Systems with Minimum Parasitic Speed Variations (in German)", *Verlag der Fachvereine an den Schweizerischen Hochschulen und Techniken*, Zürich, 1989.
13. J. Y. Hung, Z. Ding, "Design of Currents to Reduce Torque Ripple in Brushless Permanent Magnet Motors", IEE Proceedings, Vol. 140, No. 4, July 1993, pp. 260-266.
14. B.-J. Brunsbach, G. Henneberger, Th. Klepsch, "Compensation of Torque Ripple", *Electrical Machines and Drives Conf.*, Oxford, 1993, pp. 588-593.
15. H. Le-Huy, K. Slimani, P. Viarouge: "A Predictive Current Controller for Synchronous Servo Drives". *European Conference on Power Electronics and Applications (EPE)*, Florenz, 1991, pp. 2.114-2.119.
16. J. Holtz, "The Representation of AC Machine Dynamics by Complex Signal Flow Graphs". *IEEE Transactions on Industrial Electronics*, Vol. 42, No. 3, 1995, pp. 263-271.
17. J. Holtz: On the Spatial Propagation of Transient Magnetic Fields in AC Machines, *IEEE Industry Applications Society Annual Meeting*, Orlando/Fla., (1995), pp. 90-97.
18. L. Springob, "Synchronous Servo Drive with Torque Harmonic Compensation and Self-Commissioning (in German), Ph.-D Thesis, Wuppertal University, 1995.

Figure Captions

Fig. 1: Complex signal flow graph of a PM machine; p: number of pole pairs

Fig. 2: Effects of nonsinusoidal stator flux distribution; (a) and (b) complex function $\boldsymbol{\Phi}(\delta)$ of the flux linkage harmonics, (c) two-axes components of the complex function $\boldsymbol{\Phi}(\delta)$ in rotor coordinates, (d) harmonic spectrum of $\boldsymbol{\Phi}(\delta)$ in rotor coordinates

Fig. 3: Performance comparison of current controllers, (a) PI-controller with feedforward decoupling, (b) deadbeat controller; sampling frequency 10 kHz

Fig. 4: Mechanical construction of the Mavilor Discodyn ac servomotor SE 808

Fig. 5: Identification of the stator inductances following a voltage step input, (a) *d*-axis response, (b) *q*-axis response, lower trace: sampling signal

Fig. 6: Timing diagram; the *k*-values number the sampling instants

Fig. 7: Components of the rotor induced back-emf; (a) measured waveform after transformation to rotor coordinates, superscript $^{(D)}$ indicates distorted function; (b) rotor induced back-emf after nonrecursive filtering, compared with the accurate waveform obtained off-line on a test bench

Fig. 8: Identification of slot harmonic torque, (a) *q*-axis current versus rotor position angle, (b) extracted slot harmonics

Fig. 9: Signal flow diagram of the speed and torque control system (δ in degrees electrical)

Fig 10: Recorded stator current trajectories at steady-state, compensation of flux linkage harmonics. Each trajectory relates to a quarter revolution of the 8-pole machine

Fig. 11: Effect harmonic compensation; (a) compensation of slot harmonics, (b) compensation of flux linkage harmonics.

Fig. 12: Estimated machine torque at rated speed (slot ripple not included) with compensation of flux linkage harmonics, (a) PI current controller and feedforward decoupling scheme, (b) deadbeat current controller, (c) without compensation